Published in final edited form as:

Inorg Chem. 2015 November 2; 54(21): 10269–10280. doi:10.1021/acs.inorgchem.5b01576.

A Long-Lived Fe^{III}-(Hydroperoxo) Intermediate in the Active H200C Variant of Homoprotocatechuate 2,3-Dioxygenase: Characterization by Mössbauer, Electron Paramagnetic Resonance, and Density Functional Theory Methods

Katlyn K. Meier[§], **Melanie S. Rogers**[†], **Elena G. Kovaleva**[#], **Michael M. Mbughuni**[†], **Emile L. Bominaar**[§,*], **John D. Lipscomb**[†,*], and **Eckard Münck**[§,*]

[§] Department of Chemistry, Carnegie Mellon University, Pittsburgh, Pennsylvania 15213, United States

[†]Department of Biochemistry, Molecular Biology and Biophysics and Center for Metals in Biocatalysis, University of Minnesota, Minneapolis, Minnesota 55455, United States

[#] Stanford Synchrotron Radiation Lightsource, 2575 Sand Hill Road, Menlo Park, California 94025

Abstract

The extradiol-cleaving dioxygenase homoprotocatechuate 2,3-dioxygenase (HPCD) binds substrate homoprotocatechuate (HPCA) and O_2 sequentially in adjacent ligand sites of the active site Fe^{II}. Kinetic and spectroscopic studies of HPCD have elucidated catalytic roles of several active site residues, including the crucial acid base chemistry of His200. In the present study, reaction of the His200Cys (H200C) variant with native substrate HPCA resulted in a decrease in both k_{cat} and the rate constants for the activation steps following O_2 binding by > 400 fold. The reaction proceeds to form the correct extradiol product. This slow reaction allowed a long-lived ($t_{1/2}$ = 1.5 min) intermediate, H200C-$HPCA_{Int1}$ (*Int1*), to be trapped. Mössbauer and parallel mode electron paramagnetic resonance (EPR) studies show that *Int1* contains an S_1 = 5/2 Fe^{III} center coupled to an S_R = 1/2 radical to give a ground state with total spin S = 2 (J > 40 cm^{-1}) in $\mathscr{H}_{exch}=J\hat{\mathbf{S}}_1\cdot\hat{\mathbf{S}}_R$. Density functional theory (DFT) property calculations for structural models *Int1* is a (HPCA semiquinone$^{\bullet}$)Fe^{III}(OOH) complex, in which OOH is protonated at the distal O and the substrate hydroxyls are deprotonated. By combining Mössbauer and EPR data of *Int1* with DFT calculations, the orientations of the principal axes of the ^{57}Fe electric field gradient and the zero-field splitting (ZFS) tensors (D = 1.6 cm^{-1}, E/D = 0.05) were determined. This information

[*]**Corresponding Authors**, emunck@cmu.edu (E. M.), lipsc001@umn.edu (J. D. L.), eb7g@andrew.cmu.edu (E. B.).

The authors declare no competing financial interest.

Supporting Information. Figures S1-S9, Tables S1-S6; crystallographic information; Mössbauer spectra with simulations of the high-spin ferric contaminant; additional details regarding the analysis of Mössbauer spectra; ^{17}O EPR analysis, variable temperature EPR data for T = 10 K to T = 60 K (Figure S6); additional details regarding DFT analysis of various models for *Int1* (Tables S2-S6); A_{eff} angular dependence plots for Models I and II (Figure S7). This material is available free of charge via the Internet at http://pubs.acs.org.

Accession Codes

The coordinates and structure factor files have been deposited in the Protein Data Bank (PDB) [www.rcsb.org/pdb] with accession numbers: 5BWG and 5BWH.

was used to predict hyperfine splittings from bound ^{17}OOH. DFT reactivity analysis suggests that *Int1* can evolve from a ferromagnetically coupled Fe^{III}-superoxo precursor by an inner-sphere proton-coupled-electron-transfer process. Our spectroscopic and DFT results suggest that a ferric hydroperoxo species is capable of extradiol catalysis.

INTRODUCTION

The recovery of carbon from stable aromatic compounds by bacteria in the environment under aerobic conditions generally involves ring activation by the introduction of hydroxyl functional groups followed by oxidative ring cleavage.[1-4] The latter process is catalyzed by dioxygenase enzymes that utilize an active site mononuclear iron, or in rare cases other metals, to activate O_2 and to direct the incorporation of both atoms of oxygen into the substrate, opening the ring. Many examples of aromatic ring cleaving dioxygenases have been reported, but the enzymes that catalyze the cleavage of catechols and catechol derivatives are among the most extensively studied.[5-18] These studies have shown that there are two families of catechol dioxygenases, namely, the Fe^{III}-containing *intradiol* dioxygenases and the Fe^{II}-containing *extradiol* dioxygenases. The extradiol enzymes cleave the catechol ring at a position adjacent to the vicinal hydroxyl groups to yield beta-hydroxy muconic semialdehyde adducts. The mechanism of the extradiol dioxygenases has been most thoroughly studied using the enzyme homoprotocatechuate 2,3-dioxygenase (HPCD).[13-15, 19-28]

A detailed mechanistic proposal[9, 16, 29] has emerged from the structural and spectroscopic observations that the homoprotocatechuate (HPCA) substrate binds to the iron as an asymmetric chelate complex with O_2 occupying an adjacent ligand site.[15, 26, 30] Asymmetric substrate binding suggests that only one of the two catecholic hydroxyl functional groups is deprotonated upon binding, a finding later confirmed in spectroscopic studies of a related enzyme.[31] The central theme of the mechanistic proposal is that electron transfer from the substrate to the adjacent O_2 would give both species radical character. Subsequent recombination of the radicals would result in formation of an alkylperoxo intermediate. Criegee rearrangement (or the equivalent stepwise process)[32, 33] of the alkylperoxo intermediate would yield a seven-membered lactone ring, which could be hydrolyzed by the second oxygen derived from O_2 to give the ring-opened product. In support of this mechanism, the use of active site variants and alternative chromophoric substrates has allowed detection of eight reaction cycle intermediates with spectroscopic and kinetic characteristics consistent with stepwise substrate binding, O_2 binding and activation, aromatic ring-opening, and product dissociation.[13-15, 20, 22, 24-26] Furthermore, when the reaction using the slow substrate 4-nitrocatechol (4NC) was carried out in a crystal of HPCD, the proposed O_2, alkylperoxo, and product complexes were formed and trapped in different active sites within the asymmetric unit allowing their structural characterization.[15] The diagnostic radical character in both iron-bound substrate and oxygen was supported by the observation of a slight distortion of the normally planar aromatic ring of the substrate in the oxygen complex.[15, 26, 34] If this distortion arises due to single electron oxidation of the ring, then the likely electron acceptor is the iron-bound O_2. The active site iron in this complex was proposed to be in the Fe^{II} oxidation state based on the observation of relatively

long Fe-O_2 bonds. Furthermore, the structure shows that O_2 binds side-on and is properly aligned to form the alkylperoxo intermediate at the ring carbon bearing the deprotonated hydroxyl group.

The most controversial intermediate in the oxidation phase of the mechanism proposed by us and others [9, 16, 24-26, 29, 34, 35] for the wild-type enzyme is the *ferrous* biradical species (substrate $SQ^{\bullet}$)Fe^{II}(superoxo$^{\bullet}$) (SQ = semiquinone). This species might be formed by either direct electron transfer between the substrate and O_2 or by a process mediated by the iron; the evidence supporting the latter is summarized in a recent review by Fielding, Lipscomb, and Que.[28] It is important to note that no oxidation state other than Fe^{II} has ever been detected in Mössbauer studies of native HPCD for any substrate complex or intermediate trapped during single turnover reactions. In this mechanism, HPCD would formally operate without a net change in the iron oxidation state. This concept was tested by replacing the Fe^{II} with Mn^{II} or Co^{II}, both of which have significantly higher redox potentials. No significant change in steady state parameters was observed, consistent with a mechanism in which the metal is not redox active.[21, 23] However, a different result was obtained using active site mutations which introduced changes in the second sphere residues near the iron; many of these involved replacing the histidine residue at position 200 (H200).[14, 22, 24] H200 has been proposed to be involved in (i) stabilization of the biradical species by charge and hydrogen bonding interactions, (ii) steric alignment of the two substrates to facilitate rapid radical recombination, and (iii) transfer of the second hydroxyl proton from the substrate to an alkylperoxo oxygen to promote O-O bond cleavage.[14] When H200 was replaced by asparagine (H200N), and 4NC was used as the substrate, the proposed electron transfer and radical recombination reactions would appear to have slowed down or been bypassed, so that a new substrate-Fe^{III}-superoxo oxygen intermediate species was trapped.[22] This observation engendered several new types of questions regarding the nature of the reactive species and suggested that the transfer of an electron from the substrate to the O_2 might occur in a stepwise rather than a concerted process. However, the Fe^{III}-superoxo intermediate did not allow substrate ring cleavage, but rather resulted in slow ring oxidation to yield a 4NC quinone.[24] The use of HPCA in place of 4NC in the reaction of the H200N variant led to another type of intermediate in which electrons from both the substrate and the iron were transferred to the oxygen to generate an Fe^{III}-(hydro)peroxo species (H200N-$HPCA_{Int1}$).[24] In contrast to the Fe^{III}-superoxo species, this intermediate did yield a ring-cleaved product, albeit at a very slow rate compared with the native reaction.

The putative (hydro)peroxo intermediate H200N-$HPCA_{Int1}$ is significant for at least two reasons. First, its formation shows that Fe^{III} states are readily accessible in the oxygen activation phase when H200 is absent. Second, its formation demonstrates the facile electron transfer between substrate and O_2 that is at the heart of the proposed extradiol dioxygenase mechanism. However, the slow rate of HPCA ring cleavage exhibited by this variant also shows that either the resulting H200N-$HPCA_{Int1}$ is not a good model for the reactive species in the wild type (WT) enzyme or that H200 accelerates the reaction such that the intermediate Fe^{III} state is not detectable.

Earlier computational studies by Siegbahn et al.[36] and more recent ones by Neese and co-workers[37] and by Shaik, Dong and Lai[34,38] suggest potential mechanistic pathways for the

wild-type HPCD enzyme which involve Fe^{III} intermediates. Neese's work supports a mechanism whereby an Fe^{III}-superoxo intermediate is rapidly formed upon reaction of the ES complex with O_2. Subsequently, in a multistep process, H200 forms a hydrogen bond to the proximal oxygen of the superoxide. This species then attacks the C2 carbon of the substrate to generate a peroxo-bridged intermediate; this process involves the transfer of two electrons from the substrate to the Fe-O_2 fragment, one to the superoxo and one reducing the iron back to Fe^{II}. The mechanism proposed by Shaik and co-workers features a quantum mechanical hybrid state $SQ^{\bullet}$-Fe^{II}-$O_2^{\bullet}$/Fe^{III}-$O_2^{\bullet}$ (their species $^5A_2$) that is stabilized by a hydrogen bond between H200 and the superoxo as the reactive intermediate.

The analysis of the experimental data for H200N-$HPCA_{Int1}$ that might reveal the nature of its reactivity was hampered by its rather short lifetime ($t_{1/2}$ = 0.4 s at 4 °C).[24] Rapid freeze quenching of this species yielded nonuniform samples of low concentration. To improve the sample quality, we describe here the use of the cysteine variant, H200C, of HPCD. This variant yields the correct ring-cleaved product and is found to have an intermediate, H200C-$HPCA_{Int1}$ (for short *Int1*) that is spectroscopically similar to H200N-$HPCA_{Int1}$ but with a 225-fold increase in lifetime ($t_{1/2}$ = 1.5 min) (H200C-$HPCA_{Int1}$ is the spin coupled high-spin semiquinone-Fe^{III}-(hydro)peroxo complex of H200C). This remarkable stability allowed the preparation of samples containing a 10-fold higher concentration of the intermediate without the problems of heterogeneity commonly encountered when using rapid freeze quench techniques. Like H200N-$HPCA_{Int1}$, *Int1* is found to have an Fe^{III} site that is antiferromagnetically coupled to a substrate semiquinone radical to yield an S = 2 multiplet. A complete analysis of the Mössbauer and electron paramagnetic resonance (EPR) spectra of this sample is presented along with density functional theory (DFT) computations calibrated by the observed spectra and based on the high resolution X-ray crystal structure of the variant. We discuss in some detail the constraints on ^{17}O magnetic hyperfine studies imposed by the uniaxial properties of the $M_S = \pm 2$ non-Kramers doublet. These experimental, structural, and computational results strongly support a structure for *Int1* that has previously not been reported for a metalloenzyme. These studies offer new insight into the mechanism of formation and stepwise activation of an Fe^{III}-hydroperoxo species capable of oxidative aromatic ring cleavage.

Experimental and Computational Methods

Sample Preparation—*Reagents*. Biochemicals and chemicals were purchased from Sigma-Aldrich or Fisher Scientific and ^{57}Fe metal (96.8 % enriched) and $^{17}O_2$ gas (70% enriched) were obtained from Cambridge Isotopes (MA).

Production of H200C HPCD (H200C) Expression Plasmid: The H200C expression plasmid was produced via site-directed mutagenesis from a plasmid containing the *Brevibacterium fuscum* 2,3-homoprotocatechuate dioxygenase *hpcd* gene in pTrc99a as previously described.[14,47] The H200C mutation was verified by gene DNA sequence analysis (University of Minnesota Genomics Center) using the oligonucleotide primer 5'-GCACATGCGCTACGACCTGTACTC-3'.

Overexpression and Purification of H200C: H200C was overexpressed in *Escherichia coli* BL21 (DE3) and purified using methods previously described. [14,47] ^{57}Fe H200C was purified from cells grown in media containing 24 g/L casamino acids, 8 g/L yeast extract, 9.4 g/L K_2HPO_4, and 2.2 g/L KH_2HPO_4, 85 mM NaCl, and 0.5% glycerol, supplemented with 50 mg/L carbenicillin, 1 mM Mg, and 0.1 mM Ca. Iron was added as ^{57}Fe metal (100 mg) dissolved in 3 M sulfuric acid and diluted with water to <0.5 M before stepwise addition into a 10 L culture. HPCD and H200C usually had a small fraction of the active site iron in the Fe^{III} state after purification. The Fe^{III} was reduced to the active Fe^{II} state and iron was quantified as previously described.[22]

Oxygen Generating System: Millimolar concentrations of dissolved oxygen were produced using *Dechloromonas aromatica* strain RCB chlorite dismutase (Cld) (generous gift of Prof. Jennifer Dubois, Montana State University, Bozeman, MT) and sodium chlorite.[48] Cld (30 μM) was added to the H200C solution and sodium chlorite was added to the O_2-saturated (4 °C) buffer solution to provide a total of 1.2 equiv of O_2 over enzyme.

Preparation of EPR Samples: The intermediate was produced during reaction of preformed 2.3 mM H200C - 2.8 mM HPCA (1.22 equiv), Cld (28 μM) with sodium chlorite (9 mM) in a Reacti-vial with rapid stirring at 4 °C. The buffer was 200 mM MOPS, pH 7.5. An aliquot of the reaction mixture was transferred to an EPR tube, aged to 31 s and frozen in a methanol-dry ice bath.

EPR samples of the intermediate using $^{17}O_2$, or $^{16}O_2$ for direct comparison, were produced in a similar manner. Preformed 2.19 mM H200C- 2 mM HPCA was reacted with an equal volume of either $^{17}O_2$ (70 %, Cambridge Isotope Laboratories, Tewkesbury, MA) or $^{16}O_2$ saturated (1800 μM) buffer solution in a Reacti-vial with rapid stirring at 4 °C. A reaction aliquot was transferred into an EPR tube, aged and frozen in a methanol-dry ice mix.

Preparation of Mössbauer Samples: The Mössbauer sample of resting H200C (4.18 mM) was made using fully reduced enzyme as described above. The sample of the enzyme-substrate complex, H200C-HPCA was produced by adding 1.2 equiv of HPCA (5.02 mM) anaerobically to the fully reduced enzyme (4.18 mM). Mössbauer samples were prepared in 200 mM MOPS, pH 7.5.

The H200C-$HPCA_{Int1}$ Mössbauer sample was produced by addition of sodium chlorite (9.5 mM) dissolved in O_2-saturated 200 mM MOPS, pH 7.5, 4 °C to H200C (4.2 mM), HPCA (5.57 mM), and Cld (30 μM) in the same buffer. The reaction was performed in a Reacti-vial with rapid stirring at 4 °C. An aliquot was transferred to a Mössbauer cup which was frozen at 34 s in liquid nitrogen.

Steady-State Kinetics—Steady state kinetic parameters were measured by monitoring ring-cleaved product formation at 380 nm (cm^{-1}) during the reaction of H200C HPCD (16 μM) with HPCA (0.019 mM to 4.86 mM) in 50 mM MOPS, pH 7.5 at 4 °C using a stopped-flow spectrophotometer (Applied Photophysics, Leatherhead, U.K.). The experiment was performed under aerobic conditions, using air-saturated buffer (4 °C, ~ 400 μM O_2).

Presteady State Kinetics and Spectroscopy—The formation and decay of the intermediate were monitored by mixing preformed anaerobic H200C-HPCA with oxygen-saturated buffer (4 °C, ~ 1.8 mM) using a stopped-flow spectrophotometer using either photodiode array detection or photomultiplier detection at 610 nm in 50 mM MOPS, pH 7.5 at 4 °C. The reaction conditions are described in the figure legends. The time courses were fit using nonlinear regression (Applied Photophysics Pro-Data Viewer version 4.0.17) to a summed exponential expression as previously described.[12]

EPR Spectroscopy—X-band EPR spectra were recorded on a Bruker ELEXSYS-II E500 spectrometer equipped with an Oxford ESR910 cryostat for low temperature measurements and a bimodal cavity (Bruker ER4116DM) for generation of microwave fields parallel and perpendicular to the static field. All experimental data were collected under nonsaturating microwave conditions. The microwave frequency was calibrated with a frequency counter, and the magnetic field was calibrated with an NMR Gaussmeter. The temperature was calibrated with resistors (CGR-1-1,000) from LakeShore. A modulation frequency of 100 kHz and amplitude 1 mT pp was used for all spectra unless otherwise noted. SpinCount, a Windows software package (available from www.chem.cmu.edu/groups/hendrich/facilities/index.html), was used to analyze and simulate the spectra. Spin quantification was determined from double integration, relative to a CuEDTA standard for which the copper concentration was accurately determined from plasma emission spectroscopy.

Mössbauer Spectroscopy—Mössbauer spectra were recorded using Janis Research Super-Varitemp dewars that allowed studies in applied magnetic fields up to 8.0 T. Mössbauer spectral simulations were performed using the WMOSS software package (SEE Co). Isomer shifts are quoted relative to Fe metal at 298 K.

Computational Methods—The DFT calculations presented in Tables S2-S6 were performed using Gaussian '09 B.01.[49] Unless otherwise noted, calculations were performed using Becke's three-parameter hybrid functional (B3LYP) and basis set 6-311G. ^{57}Fe Mössbauer isomer shifts, δ, were calculated from the DFT charge density at the iron nucleus using the calibration from Vrajmasu et al.[50]

Results and Discussion

Kinetic Profile of H200C—An HPCA substrate titration measuring the initial velocity of the H200C-catalyzed product formation (pH 7.5, 4 °C, 380 nm) provided the following steady-state parameters: k_{cat} = 0.007 ± 0.002 s^{-1} (WT HPCD k_{cat} = 3.2 s^{-1}) [13] and K_M = 18 ± 4 μM (WT HPCD K_M = 25 μM, 22 °C).[13] Rapid mixing of the preformed H200C-HPCA complex (Figure 1, red curve) with O_2 under pseudo-first order conditions, revealed the appearance of an intermediate (*Int1*) with absorption features at 390 and 610 nm within the dead time of the stopped-flow instrument (0.8 ms) (Figure 1, blue curve). The wavelength maxima and intensity of the optical spectrum suggest that it arises from a quinone or semiquinone radical state of the bound substrate.[24] *Int1* decayed with an apparent rate constant of 0.008 s^{-1} at 4° C, showing that this is the slow step in the catalytic cycle leading to the observed steady state value of k_{cat} for the overall reaction. This observation suggests that the rate-limiting step is shifted from product release to oxygen activation in this variant.

The exceptionally long lifetime of *Int1* allowed it to be trapped in high yield for spectroscopic investigation.

X-ray Crystal Structure of H200C Variant—High-resolution X-ray crystal structures of the H200C variant in the resting state and in complex with HPCA were solved at 1.75 Å (PDB 5BWG) and 1.46 Å (PDB 5BWH), respectively (Table S1, Figures 2 and S1A-D). Comparison of the H200C and the WT HPCD structures shows that the H200C substitution does not elicit any change in protein structure globally or locally within the active site (Figure 2). Furthermore, H200C substitution also preserves the same distorted octahedral metal coordination geometry and binding mode of the substrate (Figure 2). Therefore, the observed changes in activity of the H200C variant can be attributed to the chemical and molecular (steric) properties of residue 200, and its effect on the interactions within the active site.

One distinct feature in the active site of the H200C variant, in comparison to the WT enzyme, is the new solvent molecule (WatC) in the second coordination sphere (Figures 2 and S1), which is a likely consequence of the steric void created by the shorter side chain of Cys at position 200. Similarly positioned solvent was also observed in the H200N variant structures (e.g. Figure S1 D),[39] where it is stabilized by hydrogen-bonding interactions with Y269 and the substrate-C1-hydroxyl moiety (Figure S1 C). Other crystallographically observed solvent molecules in the active site (e.g., WatA and WatB, Figure 2), present in all HPCD structures, are located 5 – 8 Å away from the substrate or O_2 binding sites and thus appear to play structural rather than mechanistic roles. The steric void may have implications for the productive orientation, conformational mobility, and reactivity of the species in the O_2-binding site. The high-resolution structure of the H200C-HPCA complex serves as a starting point for the DFT computations described below.

Mössbauer Characterization of H200C-HPCA$_{Int1}$—Figure 3A shows a zero-field, 4.2 K Mössbauer spectrum of the enzyme-substrate complex, H200C-HPCA. The spectrum exhibits a well-defined doublet having parameters typical of high-spin Fe^{II}, namely, quadrupole splitting ΔE_Q = 3.55(2) mm/s and isomer shift δ = 1.14(1) mm/s. The spectrum also reveals a minority Fe^{II} species (6% of Fe, magenta line) with ΔE_Q = 2.32(3) mm/s and δ = 1.20(2) mm/s. Figure 3B shows a spectrum of an H200C-HPCA sample frozen 34 s after incubation with O_2. It should be noted that exposure to O_2 leads to the complete disappearance of the ΔE_Q = 3.55 mm/s H200C-HPCA complex, as well as the ΔE_Q = 2.32 mm/s component, in favor of a new species with ΔE_Q = 0.97(1) mm/s and δ = 0.48(1) mm/s (*Int1*).

The isomer shift of *Int1* is characteristic of high-spin (S_1 = 5/2) Fe^{III}, and as this species yields in zero applied magnetic field a quadrupole doublet rather than a spectrum exhibiting paramagnetic hyperfine structure, the Fe^{III} must reside in a complex with integer (or zero) electronic spin.

The oxygen-exposed sample also contains a minority (6% of Fe) high-spin Fe^{II} species with parameters essentially the same as those observed for resting H200C, namely ΔE_Q = 3.25 mm/s and δ = 1.22 mm/s (we will report elsewhere detailed Mössbauer studies of H200C

and H200C-HPCA). It is possible that this minority component is also present, but not resolved, in the H200C-HPCA complex of Figure 3A. If this doublet indeed represents the resting enzyme, it should be present (as it is) in the spectrum of Figure 3B too, because the resting enzyme does not react with oxygen. The sample of Figure 3B also contains, although barely discernible, a monomeric high-spin Fe^{III} contaminant (ca. 8%, broad features near +5 mm/s and −4 mm/s); we can simulate the spectra of this species reasonably well and have subtracted its contribution from the raw data of Figures 3C, D and 4 (see Figures S2, S3 and Figure S4 for simulated spectra of the high-spin ferric contaminant along with parameters listed in the figure caption).

The properties of the applied field spectra of Figures 3 and 4 suggested to us that *Int1* should yield a parallel mode X-band EPR signal. Indeed, *Int1* exhibits a sharp feature (Figure 5 below) with a peak at $g = 8.04$ (where g is defined by $g = h\nu/\beta B$). Such a feature typically results from the $M_S = \pm 2$ doublet of an $S = 2$ multiplet for which $g \approx 2g_zS$. These observations suggest that the iron center of *Int1* is a system for which the high-spin ($S_1 = 5/2$) Fe^{III} is exchange coupled to a radical ($S_R = 1/2$). We describe the data by the Hamiltonian of eq 1.

$$\hat{\mathscr{H}} = J\hat{\mathbf{S}}_1 \cdot \hat{\mathbf{S}}_R + D_1\left[\hat{S}_{1z}^2 - \frac{35}{12} + \left(\frac{E}{D}\right)_1\left(\hat{S}_{1x}^2 - \hat{S}_{1y}^2\right)\right] + \beta\left(\hat{\mathbf{S}}_1 \cdot \mathbf{g}_1 + \hat{\mathbf{S}}_R \cdot \mathbf{g}_R\right)\cdot\mathbf{B} + \hat{\mathscr{H}}_{hf} \quad (1)$$

where $\hat{\mathscr{H}}_{hf}$ describes the hyperfine interactions of the ^{57}Fe nucleus,

$$\hat{\mathscr{H}}_{hf} = \hat{\mathbf{S}}_1 \cdot \mathbf{a}_1 \cdot \hat{\mathbf{I}} + \frac{eQV_{z'z\nabla'}}{12}\left[3\hat{I}_{1z'}^2 - \frac{15}{4} + \eta\left(\hat{I}_{1x'}^2 - \hat{I}_{1y'}^2\right)\right] - g_n\beta_n\mathbf{B}\cdot\hat{\mathbf{I}} \quad (2)$$

In eq 1, D_1 and E_1 are the axial and rhombic zero-field splitting (ZFS) parameters of the Fe^{III} ion, and $\mathbf{g}_1$ and $\mathbf{g}_R$ are the g-tensors of the Fe^{III} and the radical, respectively. For the present type of ligand coordination, namely high-spin Fe^{III} with nitrogen and oxygen ligands, $|D_1|$ is typically $\approx 1\ cm^{-1}$ (below we find $D_1 = +1.2\ cm^{-1}$). It is reasonable to assume that $\mathbf{g}_1$ and $\mathbf{g}_R$ are isotropic and that $g_1 \approx g_R \approx 2.00$. The ^{57}Fe magnetic hyperfine tensor of high-spin Fe^{III}, $\mathbf{a}_1$, is generally isotropic to within a few percent. The electric quadrupole interaction, the second term in eq 2, is written in the principal axis frame (x',y',z') of the electric field gradient (EFG) tensor. Mössbauer spectroscopists generally choose (x',y',z') such that $|V_{z'z'}| \geq |V_{y'y'}| \geq |V_{x'x'}|$. This choice confines the asymmetry parameter, $\eta = (V_{x'x'} - V_{y'y'})/V_{z'z'}$, to the range $0 \leq \eta \leq 1$. The Euler angles α, β, and γ relate the principal axis frames of the EFG and ZFS tensors; the polar angles α and β position z' in (x,y,z) and γ rotates the EFG around z'. These angles are called $(\alpha\beta\gamma)_{EFG}$ in the WMOSS software.

For *Int1* we found (see below) that the exchange coupling constant, J, is positive (antiferromagnetic coupling) and large ($> 40\ cm^{-1}$) compared to the ZFS of the ferric ion, $J >> D_1$. Under these conditions it is useful to treat the system as an isolated $S = 2$ ground multiplet and to describe it in the *coupled* representation using eq 3.

$$\hat{\mathscr{H}}_{S=2} = D\left[\hat{S}_z^2 - 2 + \left(\frac{E}{D}\left(\hat{S}_x^2 - \hat{S}_y^2\right)\right)\right] + \beta\,\hat{\mathbf{S}}\cdot\mathbf{g}\cdot\mathbf{B} + \hat{\mathscr{H}}_{hf} \quad (3)$$

The quantities of eq 3 are related to those of the uncoupled representation of eq 1 by D = (4/3) D_1, $(E/D) = (E/D)_1$, and $\mathbf{g} = (7/6)\mathbf{g}_1 - (1/6)\mathbf{g}_R$ (throughout this section, we take $g_x = g_y = 2.0$; below we find that $g_z = 2.01$). For the hyperfine interactions of the $S = 2$ multiplet, we can use equation 2 by replacing $\hat{\mathbf{S}}_1 \cdot \mathbf{a}_1 \cdot \hat{\mathbf{I}}$ by $\hat{\mathbf{S}} \cdot \mathbf{A}_1 \cdot \hat{\mathbf{I}}$; the expression $\mathbf{A}_1 = (7/6)\,\mathbf{a}_1$ relates the a_1-tensor of the local Fe^{III} site to the A_1-tensor of the coupled system, $\mathbf{A}_1$.

The red lines in Figures 3C, D and 4 A-E are spectral simulations based on eqs 1 and 2 using the parameters listed in Table 1. The spectra shown in Figures 3 and 4 are superpositions of five subspectra, one for each sublevel of the $S = 2$ multiplet. In Supporting Information we describe in detail how all the parameters of Table 1 can be isolated and determined once the origins of individual absorption lines in each spectrum are recognized under conditions of variable field and variable temperature. Of particular interest for the development of the following sections is the sharp 6-line spectrum (green) of Figure 3D, which is associated with the excited $M_S = \pm 2$ non-Kramers doublet (energy levels shown in Figure S5). This doublet yields the $g = 8.04$ EPR feature discussed in the next section. The uniaxial properties of this doublet[40] imply that only the effective z component (in the ZFS frame) of the ^{17}O magnetic hyperfine interactions is observable in parallel mode EPR at X-band. We elaborate on this point in the EPR and DFT sections.

EPR Studies of *Int1*—Next we turn to the parallel-mode EPR spectra of H200C-$HPCA_{Int1}$, which reveal a fairly sharp (1.4 mT width) feature at $g = 8.04$. An expanded view of a spectrum recorded at 21 K is shown in Figure 5A. We have recorded spectra under nonsaturating conditions (20 mW) between 10 and 60 K; a set of nine spectra were collected and wider scans are shown in Figure S6. The $g = 8.04$ feature originates from the excited $M_S = \pm 2$ doublet at energy $\varepsilon = 4D \approx 6.4\ cm^{-1}$ above the $M_S = 0$ ground state. At temperatures above 60 K, the $g = 8.04$ feature broadened and became difficult to analyze; below 10 K, the signal amplitude declined sharply due to depopulation of the $M_S = \pm 2$ doublet.

The red solid line in Figure 5A is a SpinCount simulation generated using the parameters listed in the figure caption. The peak of the resonance is positioned at $g = 8.04$ rather than $g = 8.00$. From the resonance condition $h\nu = \{(4g_z\beta B)^2 + \Delta_{\pm 2}{}^2\}^{1/2}$ we infer that the shift of the resonance from $g = 8.00$ to $g = 8.04$ is mainly due to g_z (= 2.01 in eq 3); $\Delta_{\pm 2} = 0.014\ cm^{-1}$, the splitting of the $M_S = \pm 2$ doublet for $B = 0$, shifts the resonance by a mere 0.006. The intensity of the resonance is proportional to $(E/D)^4$ and, since we know the concentration of *Int1*, we can use this relationship as a sensitive measure of E/D, yielding $E/D = 0.055$ in good agreement with the $0.03 < E/D < 0.08$ obtained from the Mössbauer analysis.[41]

Using the SpinCount software we have analyzed and simulated the set of nine spectra, using eq 1. Figure 6 shows a plot of signal × T versus T for the $g = 8.04$ resonance, where signal × T is proportional to the population of the $M_S = \pm 2$ doublet. The solid lines in Figure 6 are calculations for different values of J; the rise of the curve depends mainly on the zero-field splitting parameter D_1 and is well represented by choosing $D_1 = +1.2\ cm^{-1}$, in good agreement with the Mössbauer results. The data of Figure 6 indicate that between 15 K and 30 K the calculated population of the $M_S = \pm 2$ levels is too large if $J = 30\ cm^{-1}$; we estimate that the exchange coupling constant must be larger than about 40 cm^{-1}.

The g = 8.04 signal of *Int1* is three times narrower than the g = 8.20 feature of the (HPCA$^{\bullet}$)Fe^{III}-OOH complex H200N-HPCA$_{Int1}$, suggesting that we can probe the state of the dioxygen in *Int1* by using ^{17}O enriched O_2. The uniaxial magnetic properties of the M_S = ± 2 doublet imply that only the effective components along z are observable.[40,42] For *Int1* there are four oxygens that are potential targets for ^{17}O EPR studies, namely, O_{C1}, O_{C2} of the coordinated substrate and the two oxygens of the added O_2 (via the $^{17}O_2$ enriched gas used here).

For describing ^{17}O hyperfine interactions we add a term $\hat{\mathbf{S}} \cdot \mathbf{A}(^{17}\mathrm{O}) \cdot \hat{\mathbf{I}}_{\mathbf{O}}$ to eq 3 for each enriched O, where $\hat{\mathbf{I}}_{\mathbf{O}}$ is the spin operator of the ^{17}O nucleus (I_O = 5/2). In the limit $\beta B << D$ mixing with M_S = 0 and ±1 states can be neglected and only terms containing $\hat{S}_z$ are relevant.[40] Replacing $\hat{S}_z$ by its expectation value $\langle \hat{S}_z \rangle$ = ± 2, we obtain for each of the two electronic spin levels a nuclear Hamiltonian:

$$\mathscr{H}_{^{17}O} = \pm 2 \left(A_{xz}\hat{I}_x + A_{yz}\hat{I}_y + A_{zz}\hat{I}_z \right), \quad (4)$$

where the A_{iz} are elements of the ^{17}O hyperfine tensor in the (x,y,z) frame. Eq 4 yields for the splitting of the M_S = +2 and M_S = −2 levels[43]

$$E_{\pm 2}(m_I) = \pm 2A_{eff}\, m_I = \pm 2\left(A_{xz}{}^2 + A_{yz}{}^2 + A_{zz}{}^2 \right)^{1/2} m_I \quad (5)$$

In an EPR experiment tuned to the g = 8.04 resonance, one measures the quantity A_{eff}. In S = 2 SpinCount simulations one can pretend that $\mathbf{A}(^{17}\mathrm{O})$ is diagonal in (x,y,z) and use $\mathscr{H}_{^{17}O} = A_{eff}\hat{S}_z\hat{I}_z$. In the DFT section, we give expressions for the ^{17}O hyperfine tensor for the cases where the oxygen is either a diamagnetic ligand of iron (covalent delocalization for a hydroperoxo ligand) or a ligand with radical character (radical contribution plus covalent delocalization as would apply for the oxygens O_{C1} and O_{C2}). Using the $\mathbf{A}(^{17}\mathrm{O})$ calculated by DFT in combination with information about the orientation of the unique axis, z, as determined by Mössbauer spectroscopy, we evaluate (in Figure 10, below) the A_{eff}-value of eq 5.

Figure 5B shows parallel mode X-band EPR spectra of *Int1* recorded at 21 K for samples prepared using $^{16}O_2$ (black) and 70% enriched $^{17}O_2$ (purple). Within the noise, both resonances have the same line width (the shoulder on the high field side of the ^{17}O spectrum is probably noise from the background as there is no corresponding feature on the low field slope of the line). Figure 5C shows the resonance of the ^{17}O enriched sample together with three SpinCount simulations generated using the parameters of Figure 5A and adding the $A_{eff}\hat{S}_z\hat{I}_{z,O}$ term in the S = 2 Hamiltonian of eq 3. The green line assumes an obviously too large $A_{eff}(^{17}\mathrm{O})$ = 30 MHz (the value observed for the superoxo species of H200N-4NC$_{Int1}$),[22] the blue line assumes an again too large $A_{eff}(^{17}\mathrm{O})$ = 17 MHz (the value found for H200N-HPCA$_{Int1}$),[24] and the red line shows a simulation for $A_{eff}(^{17}\mathrm{O})$ = 7 MHz which can be taken as an upper limit for $A_{eff}(^{17}\mathrm{O})$ of *Int1*.

The lack of discernible ^{17}O hyperfine broadening seems like a disappointing result. However, as it is shown below, this result is compatible with the combined DFT/Mössbauer analysis of *Int1* that indicates the unique axis is closely aligned with the direction in which the orientation-dependent A_{eff} has a minimum.

Table 1 shows that the spin Hamiltonian parameters of H200C-HPCA$_{Int1}$ are very similar to those of the HPCA$^{\bullet}$-Fe^{III}-OOH complex, H200N-HPCA$_{Int1}$. For the latter we observed A_{eff} (^{17}O) = 17 MHz for the proximal oxygen of the hydroperoxo ligand. The same ^{17}O splitting was observed when the O_{C2} was enriched with ^{17}O.[24] The finding that $A_{eff}(^{17}O) \leq 7$ MHz in H200C-HPCA$_{Int1}$ does not rule out *Int1* as an HPCA$^{\bullet}$-Fe^{III}-OOH complex. In fact, such an assignment is suggested by our DFT and ^{17}O hyperfine analysis presented below. This assignment is also consistent with the optical spectrum of Figure 1, which is indicative of a quinone or semiquinone substrate.[24] Since the Mössbauer data show that the iron is ferric in *Int1*, the added dioxygen must be a peroxo.

The reader may wonder whether our result argues against an Fe^{III}-superoxo$^{\bullet}$ complex given that we observed $A_{eff}(^{17}O)$ = 30 MHz for H200N-4NC$_{Int1}$ (Mbughuni et al.[22] described the data in the uncoupled representation of eq 1, reporting $a_{eff}(^{17}O)$ = 180 MHz). Since ^{17}O magnetic hyperfine interactions of superoxo species are highly anisotropic, our ^{17}O result does not rule out an Fe^{III}-superoxo$^{\bullet}$ complex because the unique axis of the ZFS tensor could be along a small component of $\mathbf{A}(^{17}O)$. We address this point in sections 4.3 and 4.7 of Supporting Information. The DFT calculations presented below suggest that a (HPCA)-Fe^{III}-(superoxo) complex would exhibit strong *ferromagnetic* coupling, contrary to the $S = 2$ state found for H200N-4NC$_{Int1}$.

DFT Analysis of *Int1*—The spectroscopic analyses of *Int1* have provided ^{57}Fe fine structure and hyperfine structure parameters, a lower bound for J (antiferromagnetic, $J > 40$ cm^{-1}), and an upper bound for $A_{eff}(^{17}O)$. Guided by the above experimental results and the X-ray structure of the H200C-HPCA enzyme–substrate complex, DFT calculations were performed to assign *Int1* as one of the plausible structural candidates shown in Figure 7, which vary in terms of axial ligation, protonation, and hydrogen bonding.

We have considered the spin states $S = 2$ and 3 for three models of varying size (Figure 8), obtaining an Fe^{III}-radical solution in each case. The models differ in the number of remote second-sphere residues included in the calculations and in modifications of the acetic acid side chain of the substrate, as described in the figure caption. Model III was designed to prevent migration of the radical to Arg243 (as it occurred in Model I calculations) or to the oxygens of the carboxylate tail (as it occurred in Model II). These migrations presumably occur because other protein residues that interact with these moieties were not included due to constraints on the size of the model that can be examined computationally. Model III prevents migration by replacing the acetic acid tail group of HPCA by a methyl group. A detailed analysis is presented in section 4 of the Supporting Information, and only the principal results are listed here: (i) the iron is high-spin Fe^{III} and coordinated to a hydroperoxo ligand, (ii) the hydroperoxo proton is attached to the oxygen distal to Fe, (iii) the substrate is in a radical state with its $S_R = 1/2$ spin antiferromagnetically coupled to the $S_1 = 5/2$ spin of the Fe^{III}, (iv) both the coordinating oxygen atoms, O_{C1} and O_{C2}, of the

substrate are deprotonated, (v) while the conformation with dihedral angle ∠HOOFe = 140° (rightmost conformation in Figure 7, labeled OOH, spin density plot shown in Figure 9) emerges from the analysis as the most likely conformation for *Int1*, the other two conformations for a peroxo adduct shown in Figure 7, cannot be ruled out, and (vi) O_2 binding to the enzyme substrate complex yields an Fe^{III}-superoxo complex.

The calculated J, ΔE_Q and η values allowed us to narrow the choice for a viable model for *Int1*, namely the conformer OOH (proton on the distal O) listed in row 3 of Tables S3 and S4. The experimental data exclude ferromagnetic coupling and thus rule out models for which O_{C1} is protonated (see Table S3). The high energy and the calculated δ values argue against a hydroperoxo species in which the *proximal* O is protonated (Table S5). Table S4 lists the quadrupole splitting parameters (ΔE_Q, η) as quoted in the "proper" frame for which $|V_{x'x'}| \le |V_{y'y'}| \le |V_{z'z'}|$ such that $0 \le \eta \le 1$. It is noteworthy that all calculated EFG tensors have a large negative component along the O_{E267}-Fe-$O_{proximal}$ direction. In the deprotonated variant of Model III ($\Delta E_Q < 0$, see Table S4) this direction is aligned with the largest principal component of the EFG, $eQV_{z'z'}$. For the selected OOH conformers of the three models $A_{eff}(^{17}O)$ was obtained from DFT for the two hydroperoxo oxygens, which were ^{17}O enriched in the experiment of Figure 5, using the treatment of section 4.7 of Supporting Information. For future studies the calculated $A_{eff}(^{17}O)$ values for the coordinating O_{C1} and O_{C2} of the substrate radical have been evaluated as well. (In an exchange coupled system with the radical on the substrate, the coupling of the ^{17}O nuclei of O_{C1} and O_{C2} to the electronic radical spin S_R gives for the coupled $S = 2$ system spin a projection factor of −1/6 that differs from the factor +7/6 for the ^{17}O coupling of the oxygens of the hydroperoxo ligand to the iron spin S_1. To describe the general situation we have used an expression for A_{eff} that includes terms for the couplings of the ^{17}O nuclei with the electronic spins of both the metal and the radical (cf. section 4.7 of the Supporting Information).

The $\mathbf{A}(^{17}O)$ tensors from DFT, $\mathbf{A}_{DFT}(^{17}O)$, were expressed in the principal axis frame ($x'y'z'$) of the EFG tensor for Models I, II and III using row 3 of Table S4. Using the relation between the principal axes frames of the EFG and ZFS tensors obtained from Mössbauer ($\alpha = 58°$, $\beta = 70°$ in footnote c of Table 1), the Cartesian components of $\mathbf{A}_{DFT}(^{17}O)$ were first expressed in the ZFS frame (xyz) frame and then used to determine the splitting constant A_{eff} with eq 5. It proved to be quite instructive to fix β at 70° and plot the calculated A_{eff} along the azimuth α.

Figure 10 shows plots of $A_{eff}(^{17}O)$ *vs* α for $O_{proximal}$ and O_{distal} of the hydroperoxo ligand and for O_{C1} and O_{C2} of the HPCA ligand as obtained for the OOH conformation of Model III. There is a narrow range of α values, namely $\alpha \approx 35° - 65°$, for which A_{eff} of $O_{proximal}$ assumes values that are compatible with our experimental data, namely $A_{eff} \le 7$ MHz, and interestingly the Mössbauer result $\alpha \approx 58°$ falls into this range. The calculated A_{eff} *vs* α plots for O_{C1} and O_{C2} are quite similar, apart from a displacement of $\Delta\alpha \approx 90°$ due to the O_{C1}-Fe-O_{C2} angle of about 90°. Figure 10 shows that for $\alpha \approx 120°$ the $|A_{eff}|$ values for both $O_{proximal}$ and O_{C1} are equal to ~17 MHz, values observed for these sites in H200N-$HPCA_{Int1}$.[24] $A_{eff} < 4$ MHz for O_{distal} would be too small to cause measurable broadening of the $g = 8.04$ resonance for any α. The magnitudes of A_{eff} for Models I and II are quite similar to that obtained for Model III, except that the minima for $O_{proximal}$ occur near α =

20° (see Figure S7). Interestingly, for Models I and II the A_{eff} values of O_{C1} and O_{C2} are comparable to those of Model I, indicating that the major contribution to A_{eff} comes from covalent delocalization described by the $\hat{\mathbf{S}}_1 \cdot \mathbf{a}_1 \cdot \hat{\mathbf{I}}_O$ term; see comments in section 4.7 of Supporting Information.

Mechanistic Considerations—The HPCA substrate binds the Fe^{II} center of H200C as a dianion that is protonated at O_{C1} and deprotonated at O_{C2} and the carboxylate. Our DFT calculations presented in section 4.6 of Supporting Information suggest that the enzyme substrate (ES) complex is converted to an Fe^{III}–superoxo complex upon binding molecular oxygen. The putative superoxo complex, apparently too short-lived to be detected on the millisecond time scale, would be the precursor to *Int1*, which is proposed here to be a hydroperoxo species in which the HPCA is coordinated to the iron in the fully deprotonated radical form. Making the reasonable assumption that the substrate retains the O_{C1}-proton in the formation of the superoxo species, the transformation from the superoxo species to *Int1* can be described as the transfer of a proton and an electron from the substrate to the superoxo ligand (proton-coupled electron transfer, PCET).

Although it cannot be ruled out that the deprotonation of the substrate and protonation of the superoxo ligand involve different protons, the present analysis will focus on the PCET process between the substrate and superoxo moiety. We limit the present discussion to a model in which the second sphere residues Asn157 and Trp192 have been removed from Model III. The results of the DFT calculations are summarized in Figure 11.

The figure shows the energies (solid lines) for the $S = 3$ state (ferromagnetically coupled iron–radical states) of the (H-Substrate)–Fe^{III}–$O_2^{\bullet}$ complex (left) and the Substrate$^{\bullet}$–Fe^{III}–OOH complex, in particular the OOH···O(1) conformer of *Int1* (right). The process goes through a transition state (TS) that is located at an accessible energy of about 7.7 kcal/mol above the lowest superoxo conformation, S_{ox1}. Also shown are energies (dashed) for the antiferromagnetic states ($S = 2$) obtained for the J values determined from broken-symmetry calculations. Just as for *Int1*, the superoxo species has three conformations distinguished by different hydrogen-bonding (HB) patterns. The O_{C1}-H donates a HB to WatC in the ground conformation S_{ox1}, and to the distal O of E267 in the next conformation S_{ox2} (distance H···O_{E267} is 1.7 Å; N.B. this HB does not disrupt the HB of O_{E267} to H248 in the computation. Steric constraints would be likely to prevent a HB between O_{C1}-H and E267 in the actual enzyme active site) and to the distal O of superoxo in the highest energy conformation S_{ox3} (see Figure 11). S_{ox3} is of special interest as it places the O_{C1}-proton in an ideal position for making the transfer to the superoxo and is highest in energy probably due to the elastic strain associated with the deformations required to bring the proton donor (O_{C1}) and acceptor (distal O of superoxo) atoms together to form the hydrogen bond; we will refer to the atoms as O_D and O_A, where the subscripts D and A refer to donor and acceptor, respectively. A brief discussion of both the ET and PT aspects of the PCET process as well as their relationship follows. The TS for $S = 3$ was determined to be about 800 cm^{-1} (2.3 kcal/mol) above the initial state of the transfer (i.e., the S_{ox3} conformation) and has a structure in which O_D-H > H-O_A (see Table 2). In moving from O_D to O_A, the proton raises the energy of the redox active π-type donor orbital on the substrate and lowers the out-of-plane π^*_{out} acceptor orbital on the superoxo (see Figure 12A). This alteration

leads to a level crossing and results in the transfer of an electron. In linear approximation, the proton coordinate at the crossing depends on the initial energy difference and on the difference in the slopes. The path of the transferring proton places it into the lobe of the donor π orbital and in the nodal plane of the π^*_{out} acceptor orbital, creating a configuration that favors coupling of the proton to an electron in the π lobe of the donor orbital.

A number of observations can be made from the Mulliken spin densities (SD) listed in Table 2. (1) The Mulliken spin population of iron at the TS is nearly equal to those of iron at the initial and final states of the process. The electron transfer process is thus best described as a direct transfer between the donor and acceptor that does not proceed sequentially as in the step-wise process donor $\rightarrow$ Fe $\rightarrow$ acceptor. (2) The ^{57}Fe isomer shift (see Table 2) calculated at the TS is only marginally higher than at the terminal points (see Table 2), confirming that the iron remains in the ferric state during the transfer. (3) The transfer involves a net population of $1.15 - 0.35 \approx 1.17 - 0.38 \approx 0.8$ electrons; the complementary 0.2 electrons remain on the iron throughout the process. (4) At the TS, $1.15 - 0.96 \approx 0.61 - 0.38 \approx 0.2$ electrons have been transferred, with the major part of the charge, $0.8 - 0.2 = 0.6$, still to go, showing that the electron transfer lags the proton transfer. (5) The same conclusion can be drawn from the distribution of the orbital containing the transferring β electron at the TS (spin-down-HOMO – 1, illustrated in Figure 12B) over the substrate donor, the iron intermediary, and the O_2 acceptor (see also last row of Table 2). In general, the transition states of the ET and PT parts of a PCET process do not coincide. In the present case, the crossing of the donor and acceptor levels (Figure 12A), where the populations of these orbitals are about equal, occurs after the TS of the overall process, suggesting that the TS (level crossing) of the ET is located after the TS of the PT on the internal reaction coordinate (IRC). A detailed analysis of the correlation between the proton and electron transfer processes is given in Figure S9 of section 4.8 in Supporting Information. The contour plot of the transfer orbital at the TS of the ET (shown in Figure 12B) reveals a linear combination of the π_z donor orbital of the substrate, the d_{xz} iron orbital, and the π^*_x acceptor orbital of the superoxo. The plot nicely illustrates the role of the iron orbital in connecting the orthogonally oriented, and therefore poorly interacting, ligand components of the π_z donor and π^*_x acceptor orbitals by forming bonding combinations with both these redox active ligand orbitals. The transfer process involving the mentioned spin-down orbital may be viewed as a wave packet for which the initial amplitude on the substrate declines with a concomitant amplitude increase at the superoxo, and a nearly constant amplitude at the iron.

An important factor in the electron-transfer process is the system spin. In the $S = 3$ state the donor and acceptor orbitals of the transferring spin-down electron delocalize into the vacant down-spin 3d orbitals of the Fe^{III} ion such that these orbitals effectively overlap, resulting in a strong electronic coupling between the donor and acceptor orbitals and leading to an avoided crossing, as illustrated in Figure 12A. In the $S = 2$ state, however, where the transfer essentially involves a spin-up electron, the delocalization onto the metal is forbidden because the spin-up 3d orbitals are occupied, leading to a weaker electronic coupling (Figure 12A). The stronger coupling for $S = 3$ leads to a lower TS energy for the ET and a larger transmission coefficient than in the $S = 2$ case, both factors favoring a more efficient ET for

S = 3. The spin-state effect described here stems from the spin dependence of the electronic matrix element connecting donor and acceptor. This differs from the proposed spin effects on the hydrogen atom abstraction by Fe^{IV}=O species, which originate from energy differences between the spin terms of the electron-accepting metal ion.[44] Although the ferromagnetic coupling prevailing in the superoxo intermediates yields the ground state with the most reactive spin (*S* = 3), the spin state energetics play only a minor role in the PCET reaction considered here (Figure 11).

The studies described here allow us to draw several conclusions regarding the mechanism of the H200C variant. H200C-HPCA is active, yielding the correct ring-cleaved product, albeit with a k_{cat} that is 400 times slower than that of WT-HPCD. *Int1* is best described as a $HPCA^{\bullet}$-Fe^{III}-$(OOH)_{distal}$ species, adding a new member to the growing family of Fe^{III} intermediates in HPCD variants. The nearly complete accumulation and subsequent decay of *Int1* toward product shows that this intermediate lies on the H200C catalytic pathway and is consumed in the rate-limiting step, perhaps by the distal-to-proximal proton transfer of Scheme 1, a step that would have to proceed unsupported by His200 (cf. below).

Our DFT calculations suggest that *Int1* is formed from an *S* = 3 Fe^{III}-superoxo intermediate by an inner-sphere PCET process. Although the precursor of *Int1* has not been observed experimentally, Fe^{III}-superoxo species fitting the description have been established for H200N-$4NC_{Int1}$[22] and in the *S* = 3 synthetic complex $[(O_2)Fe(BDPP)]^0$ (BDPP=(2,6-bis(((S-2-(diphenylhydroxymethyl)-1-pyrrolidinyl)-methyl)pyridine)).[45]

The oxygen activation phase of H200C, depicted in Scheme 1, invokes a proximal-hydroperoxo species, $HPCA^{\bullet}$-Fe^{III}-$(OOH)_{prox}$, to attack the substrate radical at C2, and to ultimately form the consensus alkylperoxo intermediate. Reaction mechanisms for the WT enzyme can make use of the proton shuttling abilities of H200. Thus, the DFT studies of Neese[37] and Shaik[34] (see also Dong and Lai[38]) suggest PCET attacks on the substrate by Fe^{III}-superoxo species. The studies of Lipscomb and co-workers[16] consider fast temporary storage of the O_{C1} proton on the vicinal H200 which would generate an $HPCA^{\bullet}$-Fe^{II}-superoxo radical that rapidly recombines to form the alkylperoxo species, kinetically preventing formation of a hydroperoxo species.

Conclusion

The current study suggests that a distally protonated Fe^{III}-hydroperoxo species can form in the active site of HPCD and that extradiol ring cleavage of HPCA occurs from this intermediate or one of its successors during the reaction cycle of H200C. This reaction occurs much more slowly than that of the oxy intermediate formed during the reaction of WT enzyme with HPCA, suggesting that H200 plays an important role in either catalyzing a reaction like that of H200C or promoting a different reaction that also leads to the alkylperoxo intermediate and results in ring cleavage. Slow extradiol cleavage chemistry or a reaction that yields a nonring cleaved product are characteristic of all of the intermediates we have identified using HPCD variants.[14,22,24-26,46] These include the substrate quinone-Fe^{II}-(H)peroxo ring-cleaving intermediate formed by the Y257F variant[25,26] and $4NC^{\bullet}$-Fe^{III}-superoxo intermediate of the H200N variant.[22] The observation and characterization of these intermediates demonstrate the deep diversity of complexes that can be stabilized at nonheme

iron centers in biology. However, it also demonstrates the exquisite control that the protein environment can exercise in directing and accelerating the specific chemistry required by the organism even when using a single type of metal center ligation.

Supplementary Material

Refer to Web version on PubMed Central for supplementary material.

ACKNOWLEDGMENTS

This work is supported by National Institutes of Health Grant GM024689 (to J.D.L.), by the National Science Foundation Grant CHE-1305111 (to E.M.), and by the Biological Sciences Research Council BB/H001905/1 (to E.G.K). We acknowledge support from the National Science Foundation via EPR instrumentation grant (NSF CHE-1126268) to Dr. Michael P. Hendrich. We acknowledge Soleil Synchrotron (beamline Proxima I, St Aubin, France) and Diamond Light Source (beamline I-03, Didcot, UK) for access to synchrotron radiation facilities.

REFERENCES

1. Dagley, S. The Bacteria. Sokatch, JR.; Ornston, LN., editors. Vol. 10. Academic Press; Orlando, FL: 1986. p. 527-555.Chapter 10
2. Gibson DT, Parales RE. Curr. Opin. Biotechnol. 2000; 11:236–243. [PubMed: 10851146]
3. Gibson, DT. Microbial Degradation of Organic Compounds. Marcel Dekker; New York, NY: 1984.
4. Díaz E, Jiménez JI, Nogales J. Curr. Opin. Biotechnol. 2013; 24:431–442. [PubMed: 23122741]
5. Kojima Y, Itada N, Hayaishi OJ. Biol. Chem. 1961; 236:2223–2228.
6. Que L Jr. Lipscomb JD, Münck E, Wood JM. Biochim. Biophys. Acta. 1977; 485:60–74. [PubMed: 199266]
7. Arciero DM, Lipscomb JD, Huynh BH, Kent TA, Münck E. J. Biol. Chem. 1983; 258:14981–14991. [PubMed: 6317682]
8. Whittaker JW, Lipscomb JD. J. Biol. Chem. 1984; 259:4487–4495. [PubMed: 6323476]
9. Lipscomb JD, Orville AM. Met. Ions Biol. Syst. 1992; 28:243–298.
10. Han S, Eltis LD, Timmis KN, Muchmore SW, Bolin JT. Science. 1995; 270:976–980. [PubMed: 7481800]
11. Que L Jr. Ho RYN. Chem. Rev. 1996; 96:2607–2624. [PubMed: 11848838]
12. Vaillancourt FH, Bolin JT, Eltis LD. Crit. Rev. Biochem. Mol. Biol. 2006; 41:241–267. [PubMed: 16849108]
13. Groce SL, Miller-Rodeberg MA, Lipscomb JD. Biochemistry. 2004; 43:15141–15153. [PubMed: 15568806]
14. Groce SL, Lipscomb JD. Biochemistry. 2005; 44:7175–7188. [PubMed: 15882056]
15. Kovaleva EG, Lipscomb JD. Science. 2007; 316:453–457. [PubMed: 17446402]
16. Lipscomb JD. Curr. Opin. Struct. Biol. 2008; 18:644–649. [PubMed: 19007887]
17. Bugg TDH. Tetrahedron. 2003; 59:7075–7101.
18. Knoot CJ, Purpero VM, Lipscomb JD. Proc. Natl. Acad. Sci. U. S. A. 2015; 112:388–393. [PubMed: 25548185]
19. Miller MA, Lipscomb JD. J. Biol. Chem. 1996; 271:5524–5535. [PubMed: 8621411]
20. Kovaleva EG, Lipscomb JD. Biochemistry. 2008; 47:11168–11170. [PubMed: 18826259]
21. Emerson JP, Kovaleva EG, Farquhar ER, Lipscomb JD, Que L Jr. Proc. Natl. Acad. Sci. USA. 2008; 105:7347–7352. [PubMed: 18492808]
22. Mbughuni MM, Chakrabarti M, Hayden JA, Bominaar EL, Hendrich MP, Münck E, Lipscomb JD. Proc. Natl. Acad. Sci. U. S. A. 2010; 107:16788–16793. [PubMed: 20837547]
23. Fielding AJ, Kovaleva EG, Farquhar ER, Lipscomb JD, Que L Jr. JBIC, J. Biol. Inorg. Chem. 2011; 16:341–355. [PubMed: 21153851]

24. Mbughuni MM, Chakrabarti M, Hayden JA, Meier KK, Dalluge JJ, Hendrich MP, Münck E, Lipscomb JD. Biochemistry. 2011; 50:10262–10274. [PubMed: 22011290]
25. Mbughuni MM, Meier KK, Münck E, Lipscomb JD. Biochemistry. 2012; 51:8743–8754. [PubMed: 23066705]
26. Kovaleva EG, Lipscomb JD. Biochemistry. 2012; 51:8755–8763. [PubMed: 23066739]
27. Fielding AJ, Lipscomb JD, Que L Jr. J. Am. Chem. Soc. 2012; 134:796–799. [PubMed: 22175783]
28. Fielding AJ, Lipscomb JD, Que LJ. JBIC, J. Biol. Inorg. Chem. 2014; 19:491–504. [PubMed: 24615282]
29. Arciero DM, Lipscomb JD. JBIC, J. Biol. Chem. 1986; 261:2170–2178.
30. Vetting MW, Wackett LP, Que L Jr. Lipscomb JD, Ohlendorf DH. J. Bacteriol. 2004; 186:1945–1958. [PubMed: 15028678]
31. Vaillancourt FH, Barbosa CJ, Spiro TG, Bolin JT, Blades MW, Turner RFB, Eltis LD. J. Am. Chem. Soc. 2002; 124:2485–2496. [PubMed: 11890797]
32. Deeth RJ, Bugg TDH. JBIC, J. Biol. Inorg. Chem. 2003; 8:409–418. [PubMed: 12761662]
33. Borowski T, Georgiev V, Siegbahn PEM. J. Am. Chem. Soc. 2005; 127:17303–17314. [PubMed: 16332080]
34. Dong G, Shaik S, Lai W. Chem. Sci. 2013; 4:3624–3635.
35. Spence EL, Langley GJ, Bugg TDH. J. Am. Chem. Soc. 1996; 118:8336–8343.
36. Siegbahn PE, Haeffner F. J. Am. Chem. Soc. 2004; 126:8919–8932. [PubMed: 15264822]
37. Christian GJ, Ye S, Neese F. Chem. Sci. 2012; 3:1600–1611.
38. Dong G, Lai W. J. Phys. Chem. B. 2014; 118:1791–1798. [PubMed: 24467596]
39. Kovaleva EG, Rogers MS, Lipscomb JD. Biochemistry. 2015; 54:5329–5339. [PubMed: 26267790]
40. Griffith JS. Phys. Rev. 1963; 132:316–319.
41. Münck E, Surerus K, Hendrich M. Methods Enzymol. 1993; 227:463–479. [PubMed: 8255233]
42. Hoffman BM. J. Phys. Chem. 1994; 98:11657–11665.
43. Abragam, A.; Bleaney, B. Electron Paramagnetic Resonance of Transition Ions. Clarendon Press; Oxford: 1970.
44. Shaik S, Chen H, Janardanan D. Nat. Chem. 2011; 3:19–27. [PubMed: 21160512]
45. Chiang C-W, Kleespies ST, Stout HD, Meier KK, Li P-Y, Bominaar EL, Que L Jr. Münck, Lee W-Z. J. Am. Chem. Soc. 2014; 136:10846–10849. [PubMed: 25036460]
46. Groce SL, Lipscomb JD. J. Am. Chem. Soc. 2003; 125:11780–11781. [PubMed: 14505375]
47. Wang YZ, Lipscomb JD. Protein Expr Purif. 1997; 10:1–9. [PubMed: 9179284]
48. Krebs C, Dassama LM, Matthews ML, Jiang W, Price JC, Korboukh V, Li N, Bollinger JM Jr. Coord. Chem. Rev. 2013; 257:234–243.
49. Frisch, MJ., et al. Gaussian, Inc.; Wallingford, CT: 2009.
50. Vrajmasu V, Münck E, Bominaar EL. Inorg. Chem. 2003; 42:5974–5988. [PubMed: 12971768]

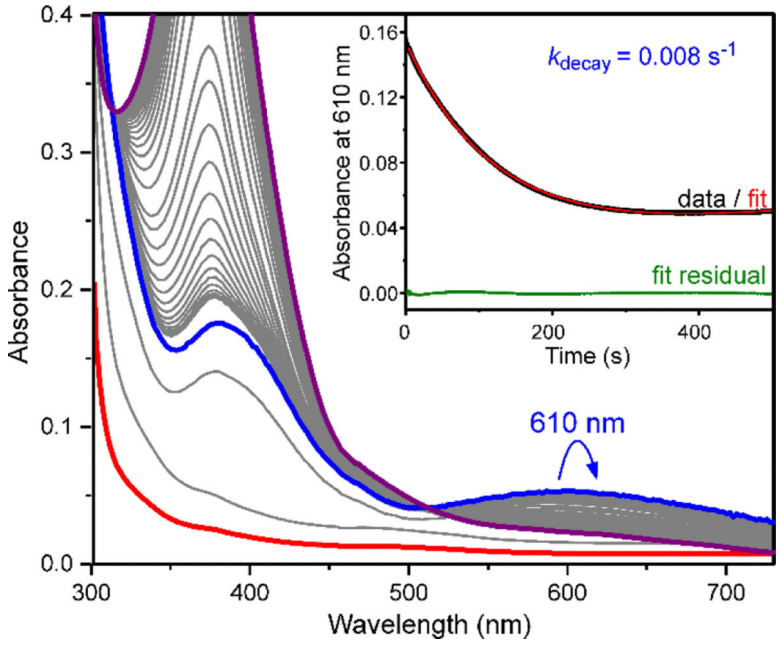

Figure 1.

Long-lived *Int1* intermediate formed during the H200C-HPCA reaction with O_2 monitored by stopped-flow spectroscopy. H200C-HPCA (440 μM) was mixed with O_2 gas-saturated buffer (1.8 mM) in 200 mM MOPS, pH 7.5 at 4 °C. Spectra were recorded between 1.26 ms and 100 s with pathlengths of 2 mm. Spectra in bold are as follows: H200C-HPCA complex, red; *Int1*, blue; final ring-opened product species, purple. **Inset:** Reduced H200C HPCD (400 μM)-HPCA (200 μM) was mixed with O_2 gas-saturated buffer (1.8 mM) in 200 mM MOPS, pH 7.5 and monitored at 610 nm using a path length of 10 mm at 4 °C. Enzyme without substrate bound does not react with O_2.

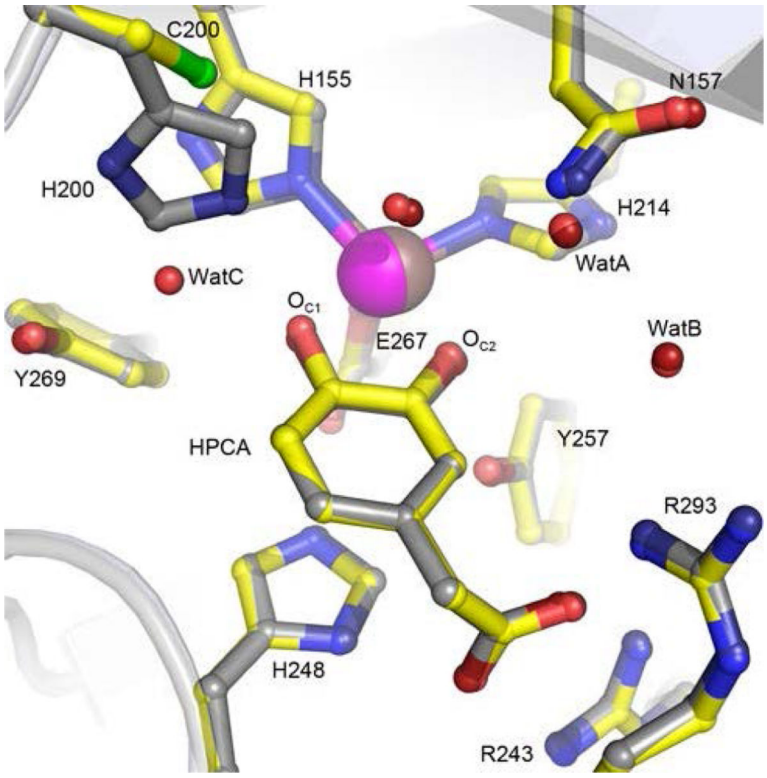

Figure 2.

Comparison of active sites of the WT HPCD and the H200C variant in complex with HPCA. Structure overlay of the WT HPCD (PDB 4GHG) and H200C (PDB 5BWH) structures. Atom color code: gray, carbon (HPCD); yellow, carbon (H200C); dark blue, nitrogen (HPCD); blue, nitrogen (H200C); dark red, oxygen (HPCD); red, oxygen (H200C); green, sulfur (H200C); bronze, iron (HPCD); purple, iron (H200C). Cartoons depict secondary structure elements for the H200C variant (gray) and HPCD (light blue). WatA-C represent crystallographically observed (not metal-coordinated) solvent in the active site.

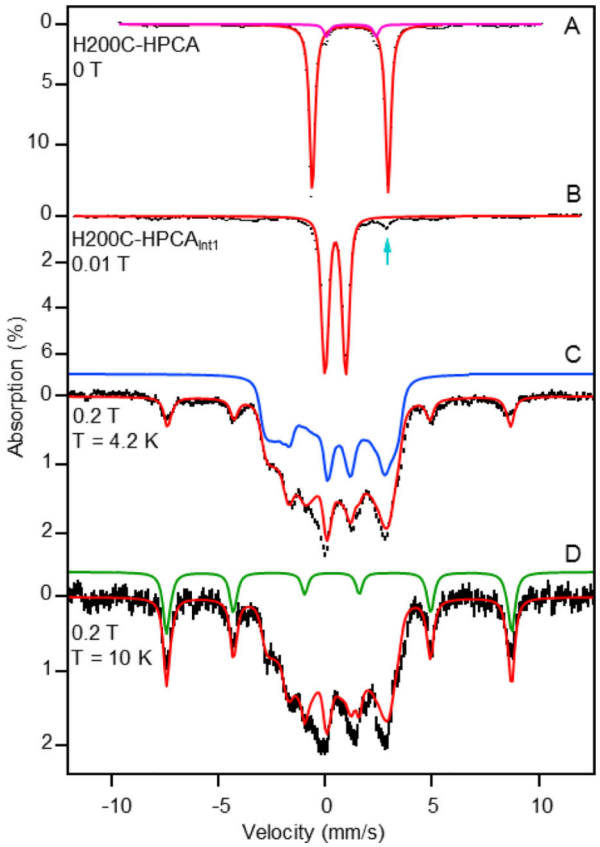

Figure 3.

(A) Zero-field, 4.2 K Mössbauer spectrum (black) of H200C-HPCA (simulation, red curve) and the minority species with ΔE_Q = 2.32 mm/s and δ = 1.20 mm/s (magenta curve). The spectra shown in panels A and B are raw data. Spectra shown in panels C and D were obtained by removing the high-spin ferric and high-spin ferrous impurities. (B, C) Spectra of the oxygenated intermediate, H200C-HPCA$_{Int1}$ = *Int1*, recorded at 4.2 K in parallel applied magnetic fields as indicated. The arrow in (B) points at the high-energy line of a doublet attributed to resting enzyme. (D) B = 0.2 T spectrum recorded at 10 K. The spectra in (C) and (D) contain a 6-line pattern (green curve) associated with the excited M_S = ±2 doublet of the S = 2 multiplet. The absorption of this feature increases with increasing temperature, showing that D > 0. The dominant contributions of the central feature, blue in (C), are from the M_S = 0 state and M_S = ± 1 doublet.

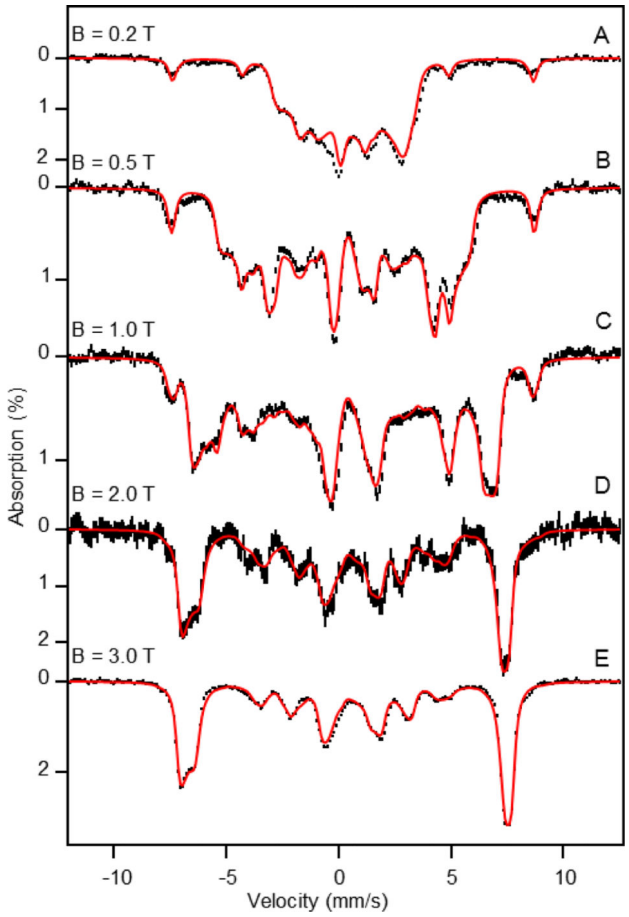

Figure 4.

4.2 K Mössbauer spectra of *Int1* recorded in variable, parallel applied magnetic fields of (A) 0.2 T, (B) 0.5 T, (C) 1.0 T, (D) 2.0 T, and (E) 3.0 T. The black hash-mark curves are the spectra that result after subtraction of simulations for the minority Fe^{II} (6%) and Fe^{III} (8%) contaminants from the raw data. The Fe^{III} contaminant was simulated with parameters given in the caption of Figure S4. Red lines are spin Hamiltonian simulations using the parameters listed in Table 1.

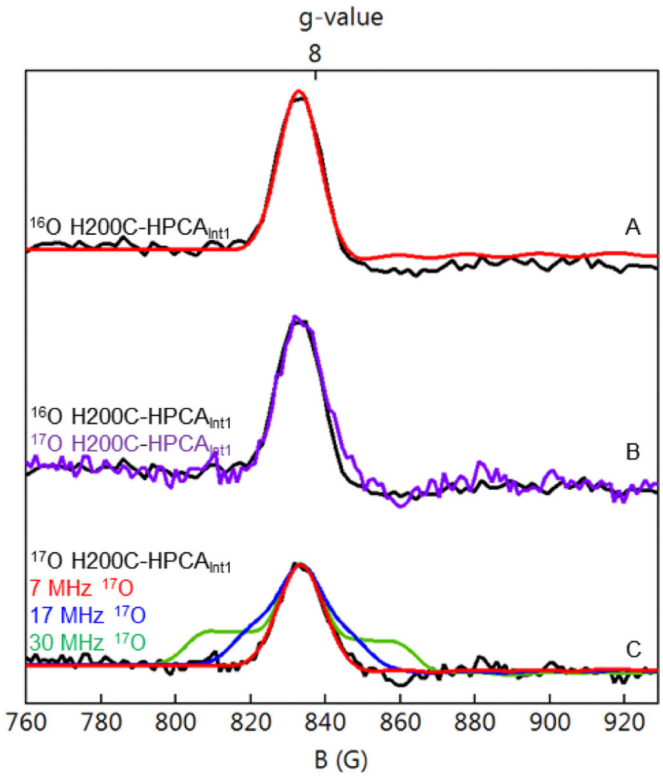

Figure 5.

Parallel mode X-band EPR spectra of H200C-HPCA$_{Int1}$ recorded at 21 K. (A) ^{16}O *Int1*, black curve. The red curve is an $S = 2$ SpinCount simulation based on eq 3 using $D = +1.6$ cm^{-1}, $E/D = 0.055$, $g_z = 2.01$, $\sigma(E/D) = 0.005$ and 0.57 mT packet line width. (B) Comparison of spectra of the ^{16}O sample of (A) (black) with a sample of *Int1* enriched with ~ 70% $^{17}O_2$ (purple curve). The purple curve has been scaled to match the peak amplitude of the $g = 8.04$ feature of the ^{16}O sample. (C) Experimental spectrum of the $^{17}O_2$ enriched sample (black) with simulations for A_{eff} (^{17}O) = 7 MHz (red), 17 MHz (blue), and 30 MHz (green). Conditions: 9.37 GHz frequency, 20 mW nonsaturating microwave power, 1 mT modulation, $T = 21$ K.

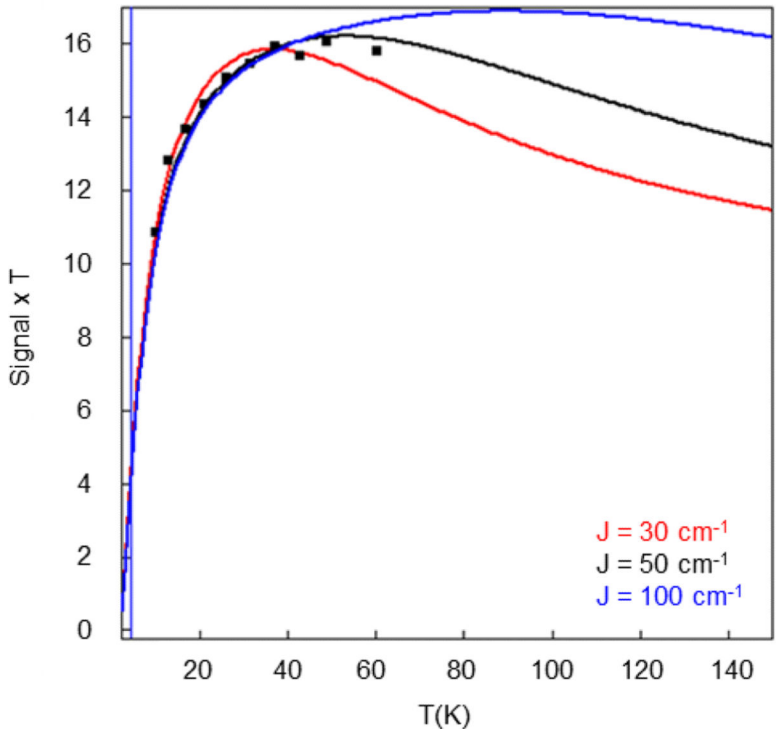

Figure 6.

(Signal × *T*) *vs T* plot of *Int1* obtained from analysis of the variable temperature parallel mode EPR signal at $g = 8.04$ shown in Figure S6.

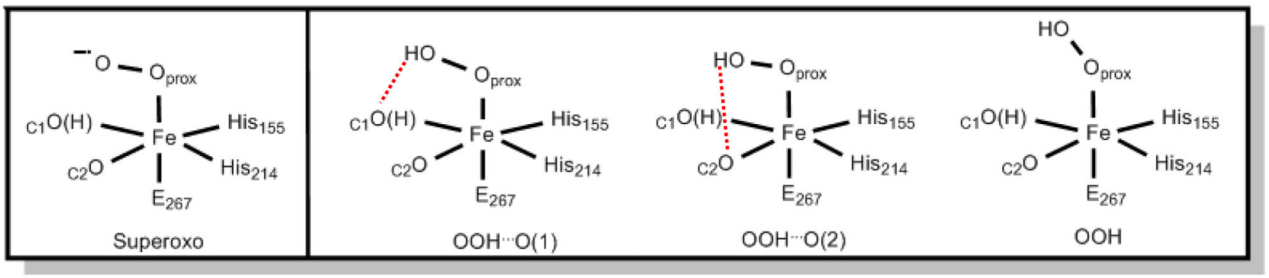

Figure 7.
Structural candidates for Fe^{III} complex *Int1*.

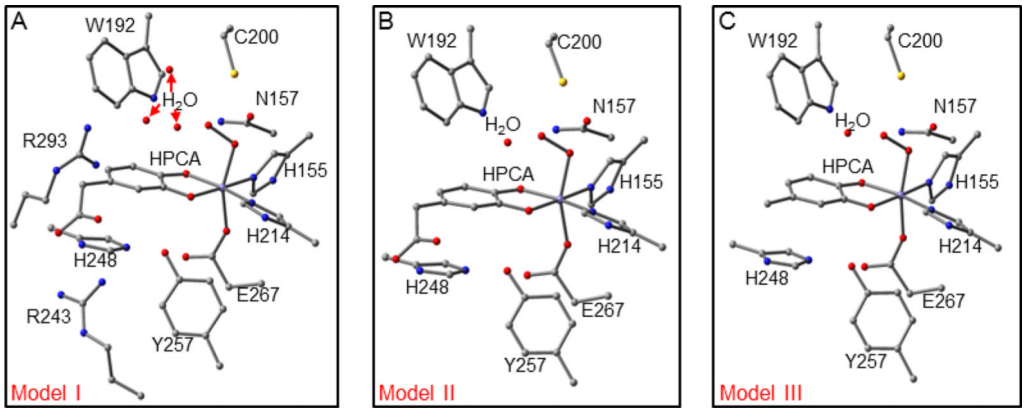

Figure 8.

DFT models for *Int1*. Panel (A) shows Model I, and includes second- and third-sphere residues Y257, H248, N157, C200, W192, R243, R293, and three crystallographic waters (WatA-C) adjacent to the active site (PDB 5BWH). Panel (B) shows Model II for *Int1*; the residues R243, R293, and two of the crystallographic waters (WatA and WatB) have been removed. Panel (C) shows Model III in which the substrate acetic acid side chain has been truncated and is replaced by a methyl group. Hydrogen atoms have been omitted for clarity.

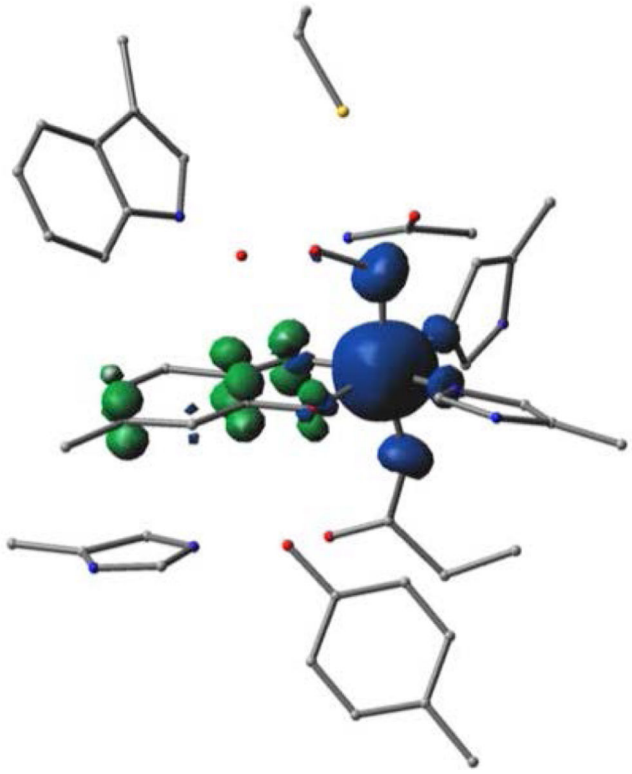

Figure 9.

Spin density plot for the OOH conformation (Figure 7, right) of Model III. Regions of blue correspond to spin-up density, and regions of green correspond to spin-down density. Note that O_{C1} and O_{C2} (in the foreground) display both spin-up and spin-down densities. Hydrogens are not shown for clarity.

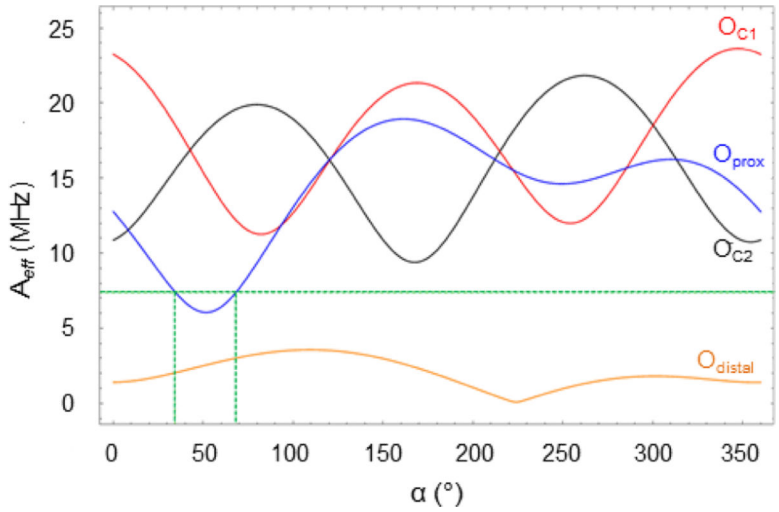

Figure 10.

A_{eff} vs α calculated for O_{C1} and O_{C2} of the HPCA substrate, and $O_{proximal}$ and proton carrying O_{distal} of the hydroperoxo ligand. The green dashed line indicates the experimentally determined upper limit for A_{eff} for the hydroperoxo oxygens. The plot was prepared using $\beta = 70°$. The DFT-calculated principal components of $\mathbf{A}(^{17}O_{proximal})$ are [−5.8, −16.2, −21.0] MHz. Angles α and β position z' of the EFG in the x,y,z frame of the ZFS tensor. Figure S8 shows the direction of the unique axis relative to the DFT structure.

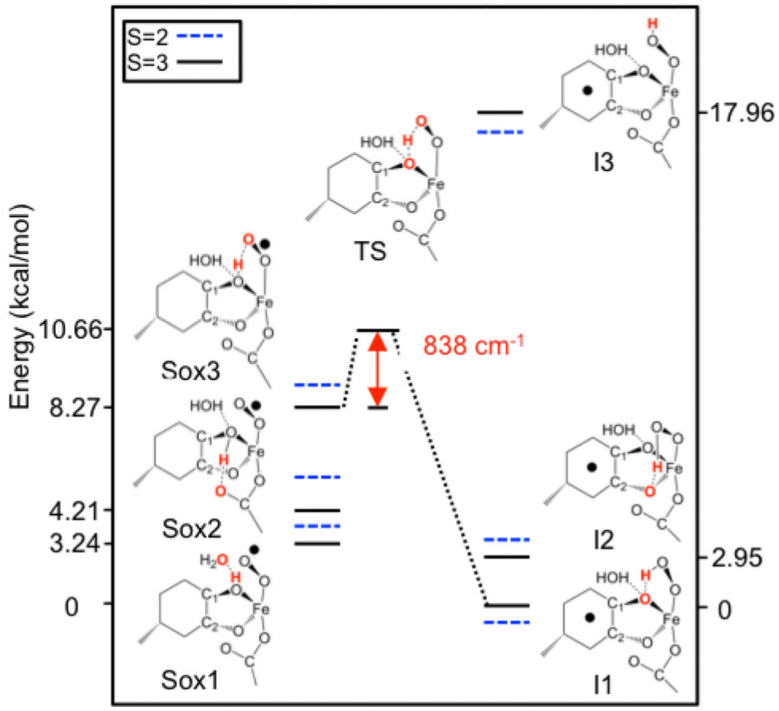

Figure 11.

Diagram depicting the DFT-calculated transformation from a superoxo species to *Int1* as described by transfer of a proton and an electron from the substrate to the superoxo ligand (proton-coupled electron transfer, PCET). The water molecule indicated is crystallographic WatC. Solid and dashed lines indicate the lowest spin septet and quintet states, respectively, for each conformation. Atoms highlighted in red are involved in hydrogen bonding interactions that affect the transfer. Energies on the left and right frame refer to the energies of the $S = 3$ states.

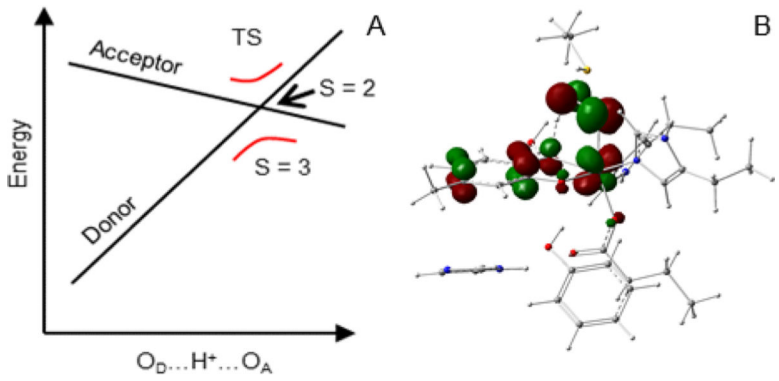

Figure 12.

(A) Schematic depicting the crossing of the donor and acceptor levels. (B) Contour plot of the orbital of the transferring spin-down electron at the level crossing where the populations of this orbital at the donor and acceptor are equal.

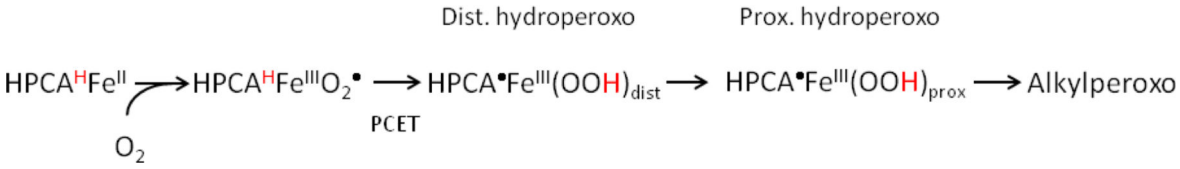

Scheme 1.

Proposed Oxygen Activation Pathway for the H200C-HPCD Variant That Involves Conversion of a Ferric Superoxo Intermediate to a Distal-Protonated Hydroperoxo, Semiquinone Radical Intermediate via Inner-Sphere PCET. [a] In the ES complex and superoxo intermediate the substrate is protonated at O_{C1} (red superscript H).

Table 1

Spin Hamiltonian Parameters, Equation 1, of Fe^{III} Species in H200C and Intermediates of H200N[a]

Intermediate	D_1 (cm^{-1})	$(E/D)_1$	J (cm^{-1})	ΔE_q (mm/s)	η	a_1[x,y,z] (T)	δ (mm/s)	Ref.
H200C-HPCA$_{Int1}$ HPCA$^{\bullet}$-Fe^{III}-OO(H)	+ 1.2(2)	0.05(3)	> +40	−0.97(1)[d]	0.55	−21.0(2) −21.5(2) −21.6(1)	0.48(1)	This work
H200N-HPCA$_{Int1}$ HPCA$^{\bullet}$-Fe^{III}-OO(H)	+ 1.1	0.12	+25(5)	−0.95[b]	0[b]	−21.5 −21.5 −21.5	0.48	24
H200N-4NC$_{Int2}$ 4NC$^{\bullet}$-Fe^{III}-OO(H)	+0.67	0.11	+40(10)	−0.87	0.8	−21.5 −21.5 −21.5	0.49	22
H200N-4NC$_{Int1}$ 4NC-Fe^{III}-$O_2^{\bullet}$	−0.59	0.20	+6(2)	−0.33	−3	−21.4 −21.4 −21.4	0.50	22
H200C-HPCA$_{Int1}$ (S=2 representation)	+1.6[c]	0.05(3)	-	−0.97	0	−24.5 −25.1 −25.2[c]	0.48	This work

[a] Spectra of the H200N-4NC$_{Int1}$, the spin coupled high-spin Fe^{III}-superoxo complex of H200N; H200N-4NC$_{Int2}$, the spin coupled high-spin semiquinone-Fe^{III}-peroxo complex of H200N.

[b] Spectra of the H200N-HPCA$_{Int1}$ were of much lower quality; η and the quoted angles ($\alpha = \gamma = 0$, $\beta = 90°$) are rather approximate.

[c] The quantities quoted are $D = (4/3)D_1$, $(E/D) = (E/D)_1$ and $\mathbf{A}_1 = (7/6)\mathbf{a}_1$.

[d] The EFG is rotated by Euler angles $\alpha = 58°$, $\beta = 70°$, $\gamma = 50°$ relative to the ZFS tensor; see text.

Table 2

Spin Population Analysis, Isomer Shift, and Distances for PCET between Substrate and Superoxo Ligands.

State	Configuration	Substrate	Fe	O_2	Rest	Sum	δ(mm/s)	O_D-H[a]	H-O_A[a]
Initial	H-Substrate Fe^{III} $O_2^{\bullet}$	0.38	4.22	1.15	0.29	6	0.56	1.037	1.507
TS		0.61	4.18	0.96	0.26	6	0.58[b]	1.273	1.163
Final	Substrate$^{\bullet}$ Fe^{III} OOH	1.17	4.22	0.35	0.25	6	0.53	1.930	0.989
βHOMO – 1 at TS		–0.59	–0.22	–0.12	–0.07	–1	–		

[a] In Å.

[b] δ = 0.59 mm/s at cross 2 in Figure S9C.